A nanodevice for rapid modulation of proliferation, apoptosis, invasive ability, and cytoskeletal reorganization in cultured cells

Yao-Ching Hung,[a] Hsu-An Pan,[b] Shih-Ming Tai[b] and G. Steve Huang*[b]

Received 12th October 2009, Accepted 20th January 2010
First published as an Advance Article on the web 10th February 2010
DOI: 10.1039/b921354f

We have fabricated a nanodevice composed of a matrix of nine nanodot arrays with various dot sizes, ranging from a flat surface to 10 nm, 50 nm, 100 nm, and 200 nm arrays. HELA, C33A, ES2, PA-1, TOV-112D, TOV-21G, MG63, and NIH-3T3 cells were seeded onto the device and cultured for three days. To evaluate the size-dependent effect of nanodot arrays on cell growth, indices corresponding to cell proliferation, apoptosis, cell adhesion, and cytoskeletal organization were defined. VD_{50} is defined as the diameter of nanodots on which 50% of the cell population remains viable. AD_{50} is defined as the diameter of nanodots on which 50% of the cell population appears to have an apoptosis-like morphology. FD_{50} is the diameter of nanodots that promotes the formation of 50% of the focal adhesions compared to cells grown on a flat surface. CD_{50} is defined as the diameter of nanodots on which cells have half the amount of microfilament bundles compared to cells grown on a flat surface. We were able to distinguish between the invasive ability of HELA *versus* later-staged C33A cells. Ovarian cancer cell lines (ES2, PA-1, TOV-112D, and TOV-21G) also exhibited differential growth parameters that are associated with cell type, grade, and stage. Modulation of the growth of MG63 cells was also achieved. More broadly, we have established a platform that can be used to assess basic parameters of cell growth. A simplified fabrication process ensures mass production and lowers cost. According to our results, the device is capable of distinguishing among cancer cell lines at various stages and also provides basic design parameters for artificial implants. Our device will serve as a convenient and fast tool for tissue engineering and cancer treatment.

Introduction

The development of invasive and metastatic properties in cancer cells is complicated.[1–4] Invasion of cancer cells begins when cells break away from the primary tumor and penetrate the surrounding tissue, followed by movement into the circulatory system, transportation through the body, and the establishment of a secondary tumor. Changes in motility and the production of enzymes that break through surrounding tissue are characteristic of invasive cancer cells. Genes such as the KCl cotransporter (KCC) family[5,6] and actinin-4[7–10] are associated with the invasive ability of cancer cells. KCl cotransport plays a crucial role in the growth and invasion of human cervical cancer, and actinin-4 is both a biomarker of cancer invasion and a prognostic indicator for cancer patients. A fast and convenient platform for cancer diagnosis should be beneficial in obtaining additional factors and parameters that control or manipulate the invasive properties of cancer cells.

Additionally, identifying an optimized surface for cell growth is very important in tissue engineering. In recent years, many researchers have modulated cell growth and apoptosis by using different materials for the surface growth or by coating surfaces with extracellular matrix (ECM) or growth factors.[11–25] Many studies indicate that nanostructures such as nanofibers, sharp tips, or nanotubes can affect cell proliferation. For example, nanofibers could guide the growth direction of cell proliferation.[20] As the nanotopographical three-dimensionality of a sharp tip is increased, consistent trends of fewer cells and a smaller cell size were observed.[12] Cell adhesion and spreading were severely impaired on nanotubule layers with a tube diameter larger than 50 nm, resulting in dramatically reduced cellular activity and a high incidence of programmed cell death.[19] In our previous studies, we have shown differential growth of NIH-3T3 cells on nanodot arrays with dot diameters ranging from 10 nm to 200 nm. Cells grew normally on the 10 nm array and on flat surfaces. However, 50 nm, 100 nm, and 200 nm nanodot arrays induced apoptotic events. The occurrence of apoptosis is mediated by the formation of focal adhesions, which can be seen using immunostaining. Thus, utilization of assemblies containing a range of nanostructures should be helpful in obtaining parameters that are useful in the design and evaluation of artificial implants for tissue engineering.

In the current study, we fabricated a nanodevice consisting of a matrix of nine nanodot arrays with various dot sizes ranging from a flat surface to 200 nm dots. We used this device to survey the basic parameters of cancer cell lines. According to our results, the device is capable of distinguishing among cancer cell lines of

[a]*Section of Gynecologic Oncology, Department of Obstetrics and Gynecology, China Medical University and Hospital, 91 Hsueh Shih Rd, Taichung, 404, Taiwan, ROC*
[b]*Institute of Nanotechnology, National Chiao Tung University, Hsinchu, Taiwan, ROC. E-mail: gstevehuang@mail.nctu.edu.tw*

various stages and also provides basic design parameters for artificial implants. Our device will serve as a convenient and fast tool for tissue engineering and cancer treatment.

Materials and methods

Chemicals

Glutaraldehyde and osmium tetroxide were purchased from Electron Microscopy Sciences (USA). Anti-vinculin mouse antibody was purchased from Abcam (USA). Alexa Fluor 594 phalloidin and Alexa Fluor 488 goat anti-mouse IgG were purchased from Invitrogen (USA). Trypsin was purchased from Sigma (USA). Polydimethylsiloxane (PDMS) was purchased from Sil-More (Taiwan). Other chemicals of analytical grade or higher were purchased from Sigma or Merck.

Fabrication of the nanodevice/matrix of nanodot arrays

Nanodot arrays were fabricated as described.[26] A tantalum nitride (TaN) thin film with a 200 nm thickness was deposited onto a 6 in silicon wafer followed by deposition of 400 nm thick aluminium on top of the TaN layer. Anodization was carried out in 1.8 M sulfuric acid at 5 V for the 10 nm nanodot array, and in 0.3 M oxalic acid at 25 V and 100 V for the 50 nm and 100 nm nanodot arrays or in 5% (w/v) phosphate acid (H_3PO_4) at 100 V for 200 nm nanodot arrays. Porous anodic alumina was formed during the anodic oxidation. The underlying TaN layer was oxidized into tantalum oxide nanodots using the alumina nanopores as a template. The porous alumina was removed by immersion in 5% (w/v) H_3PO_4 overnight. A thin layer of platinum (*ca.* 5 nm) was sputtered onto the structure to improve biocompatibility and to unify the surface chemistry. The dimensions and homogeneity of the nanodot arrays were measured and calculated from images taken using JEOL JSM-6500 TFE-scanning electron microscopy (SEM).

The fabricated nanodot arrays were cut into 1 cm × 1 cm squares and integrated into a 3 × 3 matrix that was set in a PDMS frame (Fig. 1c). The PDMS frame was molded in a glass template fabricated by photolithography.[27] Before curing, the template-covered PDMS was held for 1 h to allow all bubbles in the PDMS layer to escape. The curing process was performed by heating the PDMS to 75 °C in an oven for approximately 45 min. The final matrix contained a flat-surfaced square at the center surrounded by nanodot arrays ranging from 10 nm to 200 nm (Fig. 1c).

Cell culture

Characteristics of the cell lines are summarized in Table 1. HELA, PA-1, and MG63 cells were cultured in Dulbecco's

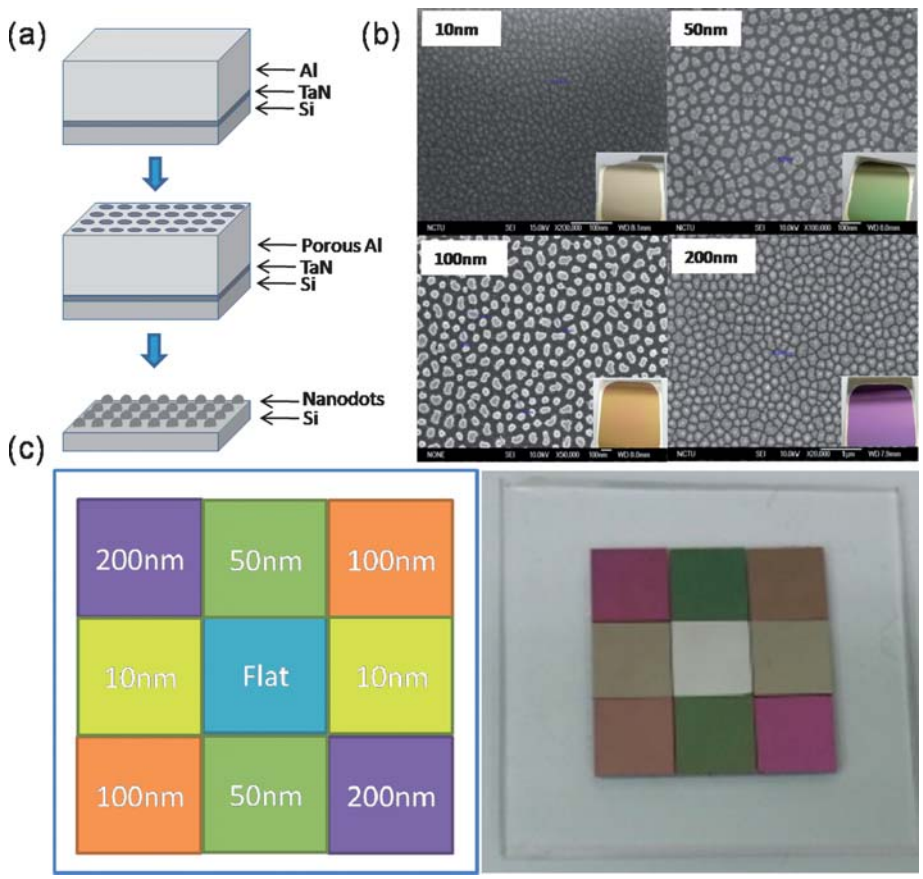

Fig. 1 Fabrication of an integrated nanodevice for screening of cellular response. (a) Schematic representation of fabrication of tantalum-based nanodot arrays using AAO processing. (b) SEM images of tantalum oxide nanodot arrays with dot diameters of 10 nm, 50 nm, 100 nm, and 200 nm constructed on a silicon wafer. (c) Schematic drawing (left) and photograph (right) of integrated nanodevice.

Table 1 Characterization of cell lines used in the current study

Cancer type	Name	Cell type	Clinical origin	Description
Cervical carcinoma	HELA	Epithelial	Adenocarcinoma	Low p53 expression, contains HPV-18
	C33A	Epithelial	Carcinoma	Negative for HPV DNA and RNA
Ovarian carcinoma	ES2	Fibroblast	Clear cell carcinoma	Low P glycoprotein expression
	PA-1	Epithelial	Teratocarcinoma	Has diploid female karyotype with a translocation between chromosomes 15 and 20.
	TOV-112D	Epithelial	Adenocarcinoma	Grade 3, stage III
	TOV-21G	Epithelial	Clear cell carcinoma	Grade 3, stage III
Osteosarcoma	MG63	Osteoblast	Osteosarcoma	Produces high yields of interferon after superinduction with polyinosinic acid, polycytidylic acid, cycloheximide and actinomycin D
	NIH-3T3	Fibroblast		Highly contact inhibited and sensitive to sarcoma virus focus formation and leukemia virus propagation

Modified Eagle's Medium (DMEM) supplemented with 10% fetal bovine serum (FBS) and incubated in 5% CO_2 at 37 °C. ES2 cells were cultured in DMEM supplemented with 10% fetal calf serum (FCS) and incubated in 5% CO_2 at 37 °C. C33A cells were cultured in MEM Alpha supplemented with 10% FBS and incubated in 5% CO_2 at 37 °C. TOV-112D and TOV-21G cells were cultured in MCDB105 and Medium199 supplemented with 15% FBS and incubated in 5% CO_2 at 37 °C.

Scanning electron microscopy

Harvested cells were fixed with 1% glutaraldehyde in phosphate buffered saline (PBS) at 4 °C for 20 min, followed by post-fixation in 1% osmium tetroxide for 30 min. Dehydration was performed through a series of ethanol concentrations (5 min incubation each in 50%, 60%, 70%, 80%, 90%, 95%, and 100% ethanol) followed by air drying. The specimens were sputter-coated with platinum and examined by JEOL JSM-6500 TFE-SEM at an accelerating voltage of 10 keV. We randomly picked five SEM pictures for each condition, and we calculated the number of abnormal cells and the total number of cells.

Immunostaining of vinculin and actin filaments (microfilaments)

Cells were harvested and fixed with 4% paraformaldehyde in PBS for 15 min, followed by three washes in PBS. The membrane was permeabilized by incubation in 0.1% Triton X-100 for 10 min. Permeabilization was followed by three PBS washes, blocking with 1% bovine serum albumin (BSA) in PBS for 1 h, and three washes in PBS. The sample was incubated with anti-vinculin antibody (properly diluted in 0.5% BSA) and phalloidin for 1 h, followed by incubation with Alexa Fluor 488 goat anti-mouse antibody for 1 h, followed by three washes in PBS. We randomly picked five fluorescent pictures for each condition and calculated the number of focal adhesions (*i.e.*, green spots of vinculin) per cell.

Results

Fabrication of an integrated nanodot array device

The 3 × 3 matrix was composed of nine nanodot arrays with dot sizes ranging from 10 nm to 200 nm. Each array was cut into a 1 cm × 1 cm square and assembled as a matrix by fitting into a preformed PDMS frame.

Nanodot arrays were fabricated by AAO processing on a tantalum-coated wafer.[26] Tantalum oxide nanodot arrays with dot diameters of 10 nm, 50 nm, 100 nm, and 200 nm were constructed using different solutions and voltages on a silicon wafer (Fig. 1a). To provide a biocompatible and unique interaction surface, platinum of *ca.* 5 nm thickness was sputter-coated onto the top of the nanodots. SEM showed diameters of 10 ± 2.8 nm, 52 ± 5.6 nm, 102 ± 9.2 nm, and 212 ± 18.6 nm for 10 nm, 50 nm, 100 nm, and 200 nm dot arrays, respectively (Fig. 1b). The dimensions of the nanodots were well-controlled and highly defined.

The fabricated nanodot arrays were cut into 1 cm × 1 cm squares and integrated into a 3 × 3 matrix set on a PDMS frame (Fig. 1c). The PDMS frame was molded on a glass template fabricated by photolithography.[27] The final matrix contains a flat-surfaced square at the center with surrounding nanodot arrays ranging from 10 nm to 200 nm (Fig. 1c).

Assessment of proliferation, apoptosis, cell adhesion, and cytoskeleton reorganization for cultured cells

To define parameters that modulate the growth state of cells and to assess the cellular response against a varied nanostructured surface, the integrated nanodevice was first placed in the cell culture dish. HELA, C33A, ES2, PA-1, TOV-112D, TOV-21G, MG63, and NIH-3T3 cells were seeded on the device and cultured for three days (Table 1). Among them, NIH-3T3 cells were incorporated as a control cell line for normal fibroblasts. Cell density was counted to examine the viability of cells, and SEM was performed to assess the morphological changes of cells (Fig. 2). To evaluate cell adhesion and cytoskeletal reorganization, immunostaining specific to vinculin and actin filaments (microfilaments) was performed (Fig. 3 and 4).

To evaluate the size-dependent effects of nanodot arrays on cell growth, indices corresponding to cell proliferation, apoptosis, cell adhesion, and cytoskeletal organization were defined. VD_{50} is defined as the diameter of nanodots on which 50% of the cell population remains viable compared to cells seeded on a flat surface after 3 days of incubation. VD_{50} for each cell line was derived by counting the number of cells on the nanodot arrays, drawing the graph of viability *versus* dot diameter, and calculating the dot diameter at which 50% viability was obtained (Fig. 5).

AD_{50} is defined as the diameter of nanodots on which 50% of the cell population appears to display apoptosis-like morphology

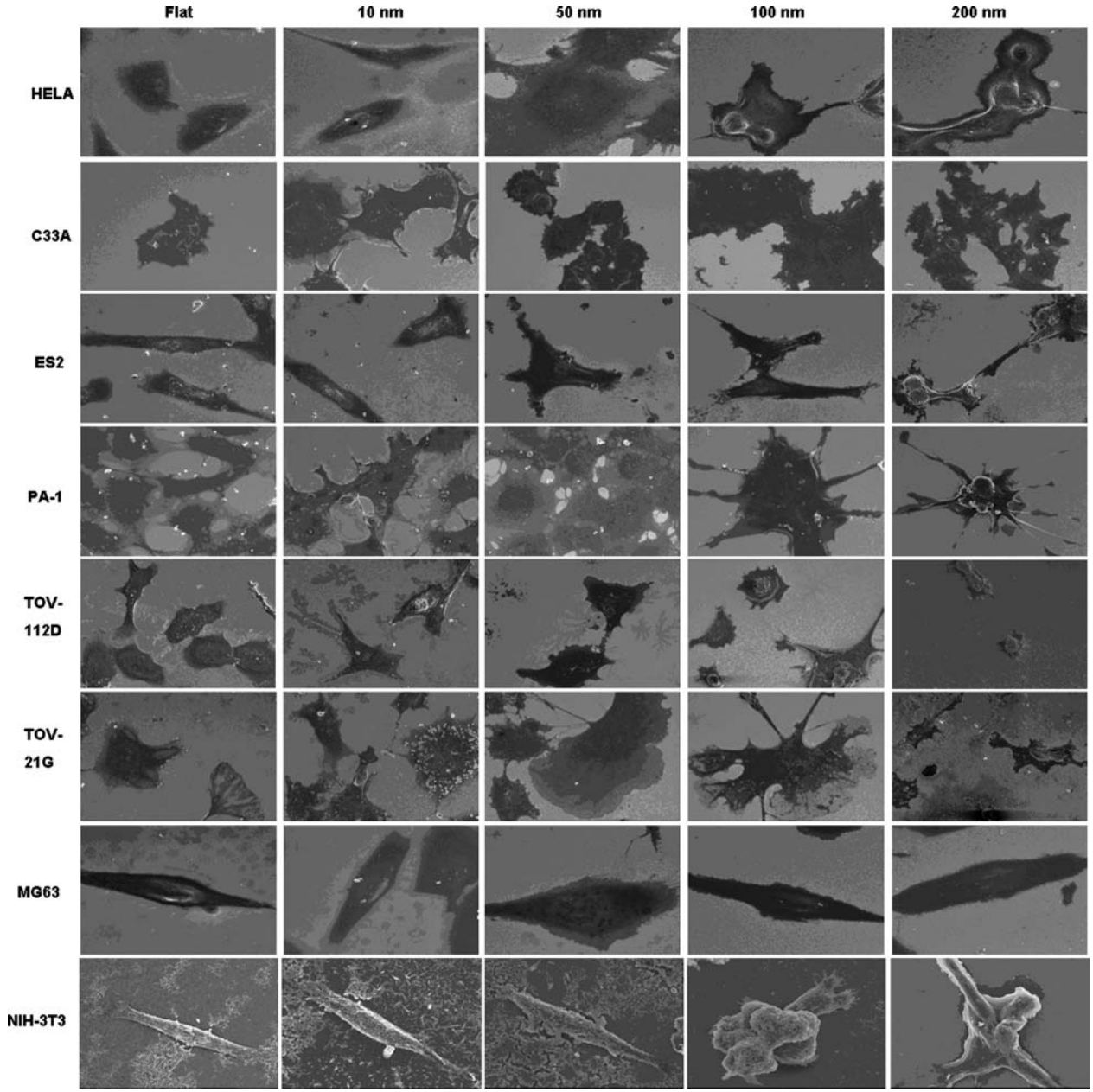

Fig. 2 SEM images of cells seeded on nanodot arrays. HELA, C33A, ES2, PA-1, TOV-112D, TOV-21G, MG63, and NIH-3T3 cells were seeded on a flat silicon surface and a 10 nm nanodot array, 50 nm nanodot array, 100 nm nanodot array, and 200 nm nanodot array. Cells were harvested at 72 h (day 3) after seeding. Representative SEM images are shown.

after 3 days of incubation. AD_{50} was calculated by counting the percentage of apoptotic cells on the nanodots, drawing the graph of percent apoptotic cells *versus* dot diameter, and calculating the dot diameter that causes 50% apoptosis (Fig. 6).

FD_{50} is the diameter of nanodots that promotes the formation of 50% of the focal adhesions compared to cells grown on a flat surface. FD_{50} was calculated by counting the number of vinculin stained spots per cell, drawing the graph of percent focal adhesions *versus* dot diameter, and finding the diameter that promotes 50% of focal adhesions compared to a flat surface (Fig. 7).

CD_{50} is the diameter of nanodots on which cells exhibit half the number of microfilament bundles compared to cells grown on a flat surface. Microfilaments (or actin filaments) are the thinnest filaments of the cytoskeleton found in the cytoplasm of all eukaryotic cells. Actin filaments are assembled in two general types of structures: bundles and networks. These structures are regulated by many other classes of actin-binding proteins. With confocal microscopy, an estimation for the number of microfilament bundles can be obtained by building a 3-d cell image. CD_{50} was calculated by counting the number of microfilament bundles per cell, drawing the graph of microfilament bundles *versus* dot diameter, and obtaining the diameter that gives a two-fold reduction in the amount of microfilament bundles compared to cells grown on a flat surface (Fig. 8).

Table 2 summarizes VD_{50}, AD_{50}, FD_{50}, and CD_{50} scores for all cell lines employed in the current study.

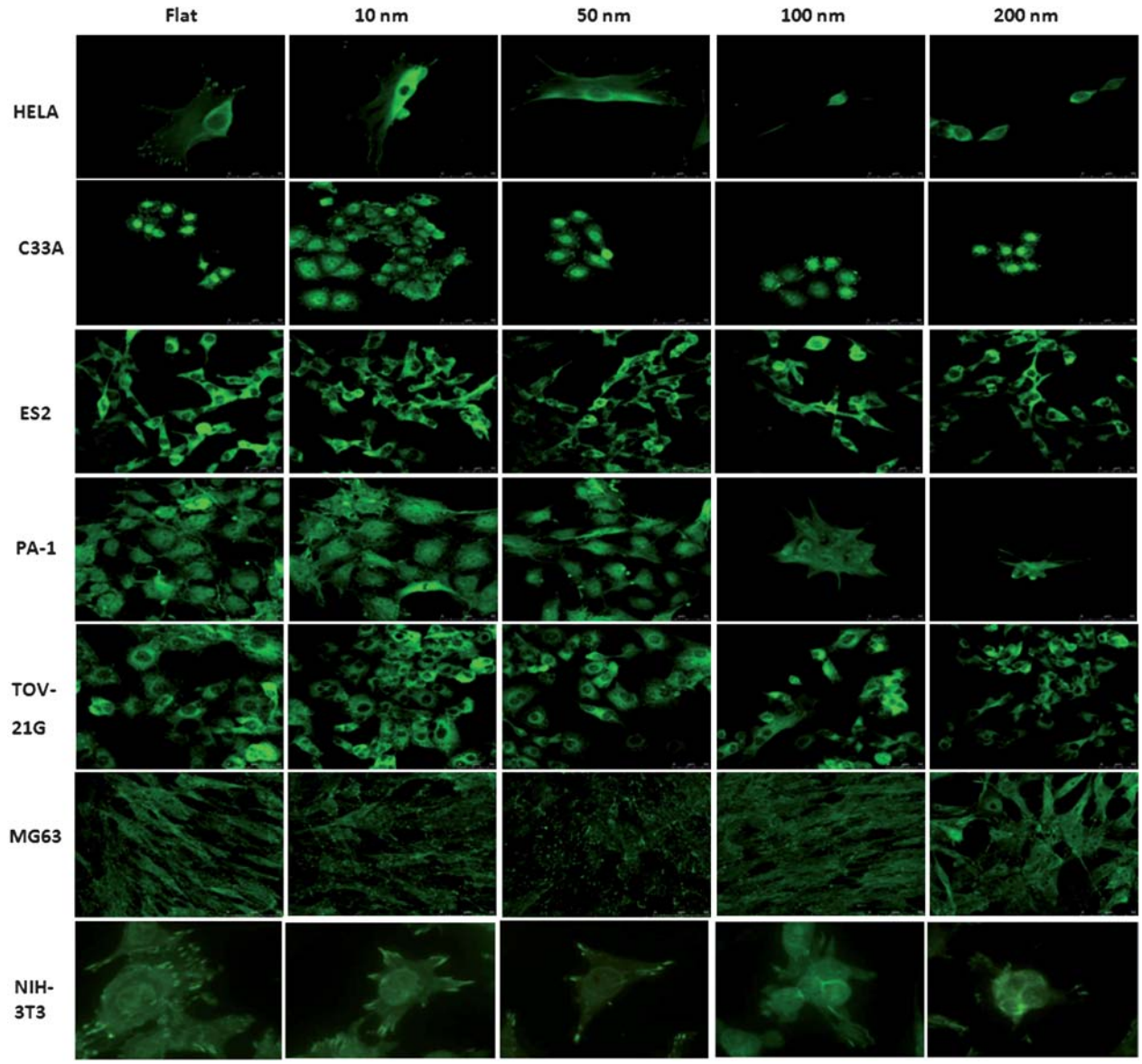

Fig. 3 Immunostaining for distribution of vinculin in cells cultured on 10 nm, 50 nm, 100 nm, and 200 nm nanodot arrays and on a flat surface. Cells were seeded on arrays for 72 h before harvest. The sample was incubated with anti-vinculin antibody (properly diluted in 0.5% BSA), followed by incubation with Alexa Fluor 488 goat anti-mouse antibody.

NIH-3T3 cells, used as a normal control cell line in the current study, are a mouse embryonic fibroblast cell line established from an NIH Swiss mouse embryo. They are highly contact inhibited and are sensitive to sarcoma virus focus formation and leukemia virus propagation. This cell line was established from NIH Swiss mouse embryo cultures in the same manner as the original random-bred 3T3 and the inbred BALB/c 3T3. Viability was at 78% and 74.2% for 10 nm and 50 nm nanodots respectively, but dropped to 30.4% and 35% for 100 nm and 200 nm nanodot arrays respectively. VD_{50} for NIH-3T3 is 71 nm. The percentage of apoptosis-like cells was 58.3% for 100 nm and reached 78.3% for the 200 nm dot array. AD_{50} for NIH-3T3 is 75 nm. The vinculin staining indicated the density of focal adhesions, which dropped to 68.8% at 50 nm and decreased to 54.6% and 46.8% for 100 nm and 200 nm respectively. FD_{50} for NIH-3T3 is 110 nm. The cytoskeletal organization lost its order when the array size was larger than 100 nm. CD_{50} for NIH-3T3 is 148 nm. The NIH-3T3 cell line grew well on flat, 10 nm, and 50 nm surfaces, but dropped to apoptotic levels and lost cell adhesion if the nanodot size was larger than 100 nm.

HELA cells are a human cervical cancer cell line carrying human papillomavirus-18 (HPV-18), with a low level of p53 expression. HELA cells are an immortal cell line used in scientific research. Viability was maintained at 91.7% for 50 nm, but it dropped to 43.2% when the nanodot size reached 100 nm, and further dropped to 24.4% for the 200 nm nanodot array. VD_{50} for HELA cells is 112 nm. The cell morphology remained flat and extended at 50 nm, but mounted and changed to an apoptosis-like shape for 100 nm and 200 nm surfaces. AD_{50} for HELA cells is 85 nm. Immunostaining indicated enhanced staining of vinculin, which represented enhanced cell adhesion for sizes under 50 nm. FD_{50} for HELA cells is 51 nm. The cytoskeletal

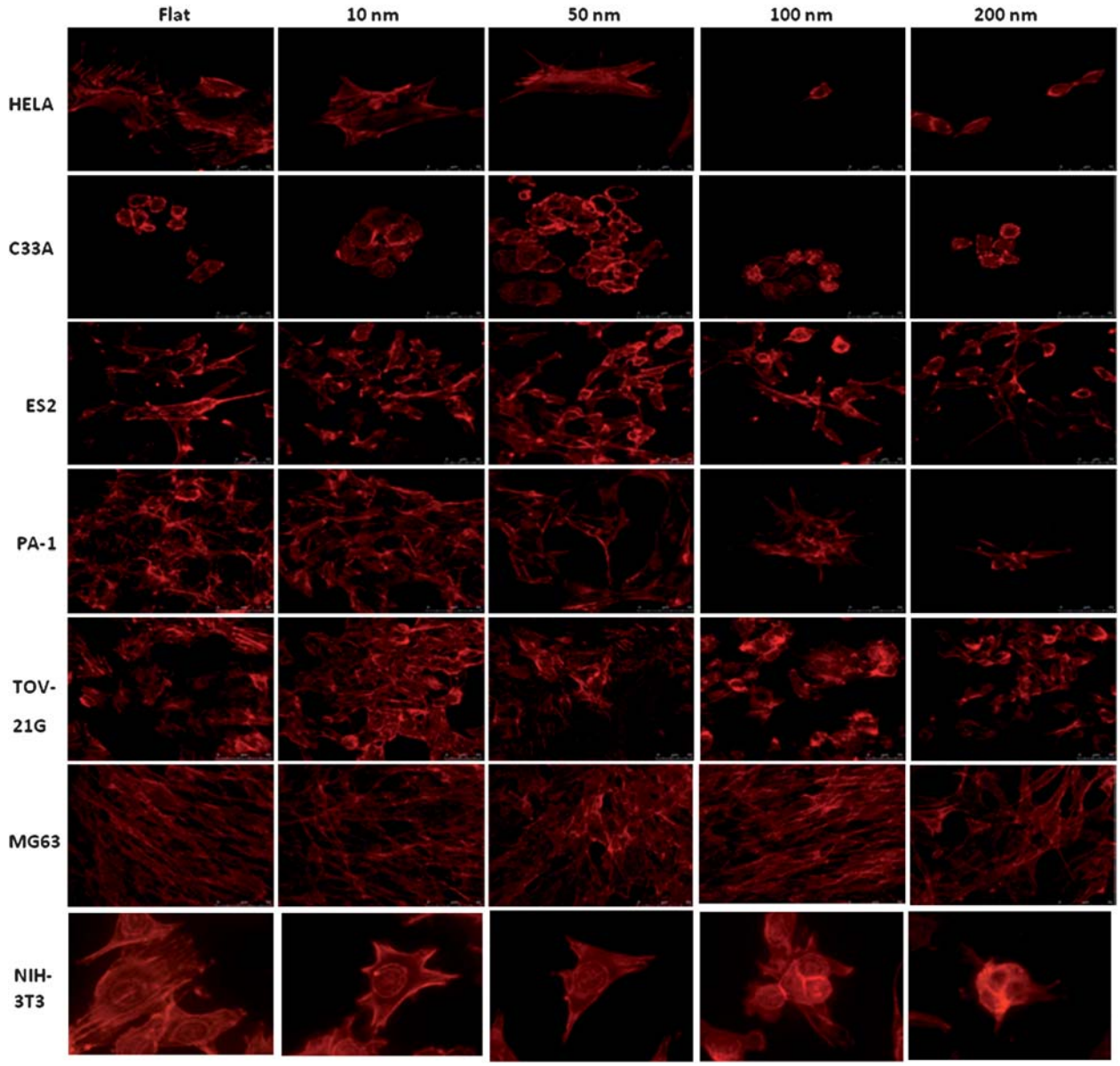

Fig. 4 Immunostaining for distribution of microfilaments in cells cultured on 10 nm, 50 nm, 100 nm, and 200 nm nanodot arrays and on a flat surface. Cells were seeded on arrays for 72 h before harvest. The sample was incubated with phalloidin.

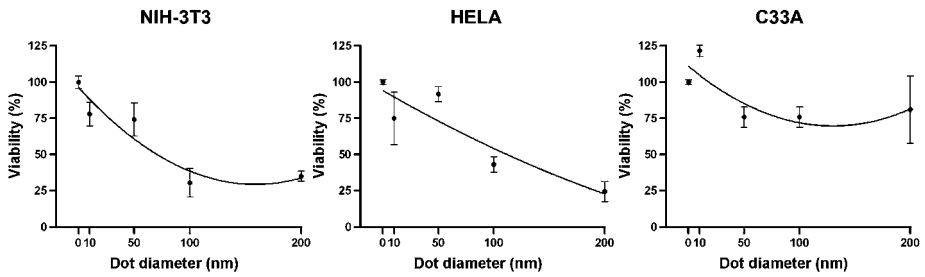

Fig. 5 Viability *versus* dot diameter for cells cultured on the nanodevice. Cells are cultured on the nanodevice for 3 days. The viable cells are counted and percent viability relative to cells cultured on a flat surface (0 nm) is calculated and graphed against the nanodot diameter. The graphs show viability of NIH-3T3 (left), HELA cells (center), and C33A (right). Each value is averaged from at least 6 independent experiments. The error bars are the standard errors. The curves for best fit are derived using SigmaPlot software.

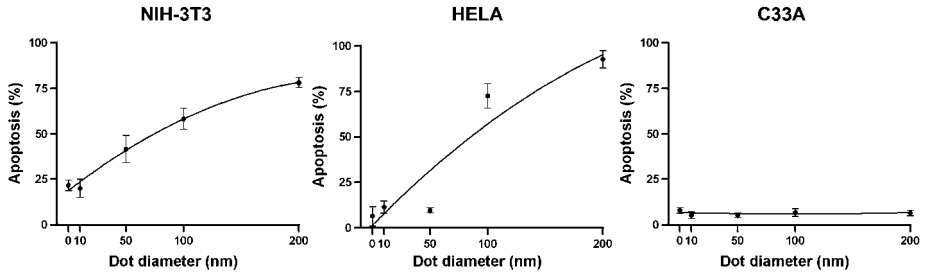

Fig. 6 Percentage of cells that have undergone apoptosis *versus* dot diameter for cells cultured on the nanodevice. Cells are cultured on the nanodevice for 3 days and SEM images are taken. Cells of apoptosis-like morphology are counted and percent apoptosis is calculated and then graphed against the nanodot diameter. The graphs show percent apoptosis of NIH-3T3 (left), HELA (center), and C33A (right) cells. Each value is averaged from at least 6 independent experiments. The error bars are the standard errors. The curves for best fit are derived using SigmaPlot software.

organization lost its order when the size was larger than 100 nm. CD_{50} for HELA cells is 94 nm. In summary, HELA cells grew well and reached optimized conditions at 50 nm, but lost cell adhesion and switched to an apoptotic mode when the dot size was larger than 100 nm. Compared to NIH-3T3 cells, HELA cells exhibited higher VD_{50} and AD_{50} but had lower FD_{50} and CD_{50}. Although HELA cells proliferated better than NIH-3T3 cells on the nanosurfaces, the cytoskeletal organization associated with the formation of focal adhesions appeared to be less tolerable to changes in nanosurfaces.

C33A cells represent a human cervical cancer cell line derived from advanced carcinoma with highly invasive activity and with negative expression for HPV DNA and RNA. No significant difference in proliferation was observed among all nanodot arrays, from flat to 200 nm. The cell morphology remained flat and extended at all sizes of the nanodot arrays. The immunostaining showed no significant difference in the number of focal adhesions. Cells grown at all conditions displayed well-organized cytoskeletons. All indices are higher than 200 nm. Compared to HELA cells, C33A cells proliferated and developed well-organized focal adhesions and cytoskeletons on all sizes of nanosurface. This cell behavior might be an indication that C33A is derived from cervical cancer that is at a later stage than the cancer from which HELA cells were derived.

The ES2 cell line was established from a surgical tumor specimen taken from a 47-year-old black woman. The tumor was described as a poorly differentiated ovarian clear cell carcinoma. This cell line exhibits low to moderate resistance to a number of chemotherapeutic agents including doxorubicin, cisplatin, carmustine, etoposide, and cyanomorpholinodoxorubicin (MRA-CN). It also expresses low levels of P glycoprotein. The viability for ES2 cells dropped to 61.3% for 100 nm and to 70.9% for 200 nm nanodots. The morphology was extended on surfaces ranging from a flat surface to 100 nm nanodots. The morphology indicated that apoptosis occurred when the nanodot size reached 200 nm. Immunostaining of vinculin showed that the number of focal adhesions decreased dramatically when cells were grown on a 200 nm dot array, and cytoskeletal organization became disordered at 200 nm. VD_{50}, AD_{50}, FD_{50}, and CD_{50} for ES2 are >200, 198, >200, and >200 nm, respectively. In summary, ES2 cells grew well on a flat surface and on nanodots up to 100 nm, but showed apoptosis and loss of cell adhesion at 200 nm.

The human ovarian teratocarcinoma cell line PA-1 was isolated from the ascites fluid of a 12-year-old girl suffering from recurrent malignant teratocarcinoma. Malignant ovarian teratocarcinomas differ from their benign counterparts in that they are a rare form of tumor and usually occur in prepubertal females. They consist of many immature elements and can arise by several mechanisms, including failure of meiosis I or II or fusion of two ova. High passage PA-1 cells are tumorigenic in nude mice upon subcutaneous injection, form embryoid bodies under nonadherent culture conditions, and form colonies in soft agar. Cytogenetically, PA-1 has a stable diploid female karyotype with a single balanced translocation between chromosomes 15 and 20. Cell viability was enhanced and rose to 107.6% on surfaces with 50 nm nanodot arrays, but decreased to 30.2% when the nanodot size reached 100 nm, and further decreased to 12.6% at 200 nm. The morphology remained flat and extended until 50 nm, but mounted and began to exhibit apoptosis on surfaces with nanodots between 100 nm and 200 nm. Decreased staining of vinculin was observed, which indicated decreased cell adhesion for nanodot sizes larger than 100 nm. The cytoskeletal organization was less ordered when the dot size was greater than 100 nm. VD_{50}, AD_{50}, FD_{50}, and CD_{50} for PA-1 are 108, 147, 72, and 142 nm, respectively. In summary, PA-1 cells grew well and reached optimized conditions on 50 nm arrays, but displayed apoptosis and loss of cell adhesion if the nanodot size was larger than 100 nm. PA-1 exhibited an earlier-staged cancerous behavior compared to the ES2 cell line.

TOV-112D cells represent a human ovarian cancer cell line derived from an endometrioid epithelial carcinoma from a 42-year-old female. It is a primary malignant adenocarcinoma of grade 3 and staged as IIIC. Viability did not change for cells grown on a flat surface to 50 nm nanodot arrays, but it decreased to 70% when the nanodot size reached 100 nm, and dropped to 50% at 200 nm. The morphology remained flat and extended at 50 nm, but mounted and showed apoptosis on 100 nm and 200 nm dot arrays. VD_{50}, AD_{50}, FD_{50}, and CD_{50} for TOV-112D are 198, 127, >200, and >200 nm, respectively. In summary, TOV-112D cells grew well on flat, 10 nm, and 50 nm surfaces, but apoptosis occurred if the nanodot size was larger than 200 nm. TOV-112D exhibited characteristics of late-stage cancer.

TOV-21G cells are a human ovarian cancer cell line. These cells are from a clear cell epithelial carcinoma derived from a 62-year-old female. This is a primary malignant adenocarcinoma, of grade 3 and staged as III. Viability was enhanced and reached 110% when grown on 50 nm nanodot arrays, but decreased to 90% when the array size was 100 nm, and to 60% at 200 nm. The

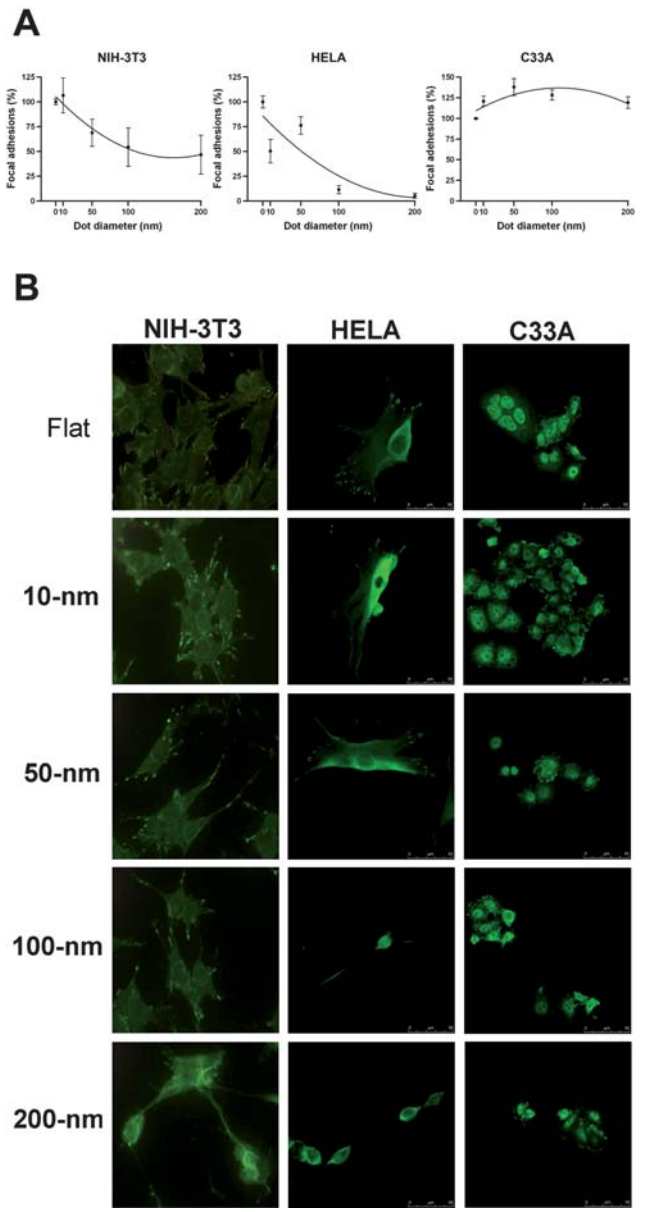

Fig. 7 Percentage of focal adhesions *versus* dot diameter for cells cultured on the nanodevice. Cells are cultured on the nanodevice for 3 days and immunostaining using anti-vinculin antibody is performed. Number of vinculin stains per cell is counted and percent focal adhesions relative to cells grown on a flat surface is calculated and then graphed against nanodot diameter (A). The graphs show percent focal adhesions of NIH-3T3 (left), HELA (center), and C33A (right) cells. Each value is averaged from at least 6 independent experiments. The error bars are the standard errors. The curves for best fit are derived using SigmaPlot software. Representative images used in the measurement are shown in (B).

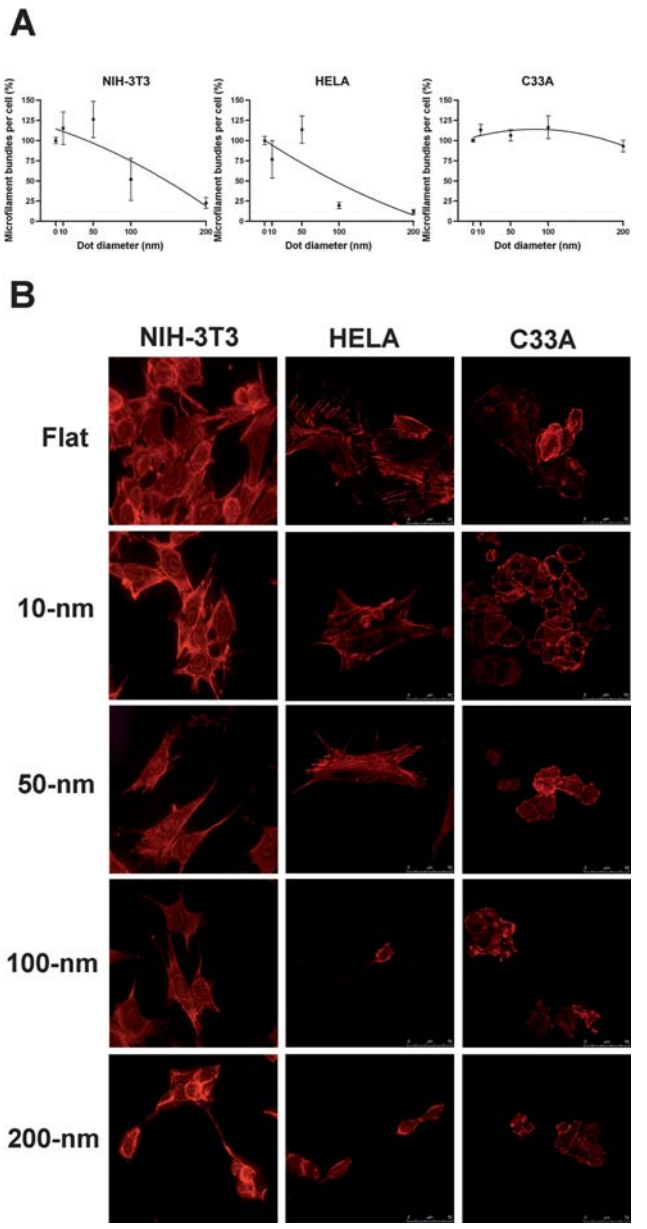

Fig. 8 Percentage of microfilament bundles per cell *versus* dot diameter for cells cultured on the nanodevice. Cells are cultured on the nanodevice for 3 days and phalloidin staining is performed. 3-D fluorescence images are obtained using a confocal microscope. The number of microfilament bundles per cell is counted and percent microfilament bundles relative to cells grown on a flat surface is calculated and graphed against nanodot diameter (A). The graphs show percent actin filaments of NIH-3T3 (left), HELA (center), and C33A (right) cells. Each value is averaged from at least 6 independent experiments. The error bars are the standard errors. The curves for best fit are derived using SigmaPlot software. Representative images used in the measurement are shown in (B).

morphology remained flat and extended at 50 nm, but mounted and showed apoptosis on the 100 nm and 200 nm dot arrays. Immunostaining indicated slightly enhanced staining of vinculin for sizes under 50 nm. The cytoskeletal organization loses order when the size is larger than 100 nm. VD_{50}, AD_{50}, FD_{50}, and CD_{50} for TOV-21G are >200, >200, 68, and >200 nm, respectively. In summary, TOV-21G cells grew well on flat, 10 nm, and 50 nm surfaces, but became apoptotic and showed loss of cell adhesion if the size was larger than 200 nm.

MG63 cells, a cell line derived from an osteosarcoma, produce high yields of interferon after superinduction with polyinosinic acid, polycytidylic acid, cycloheximide, and actinomycin D. Studies using MG63 cells provide some important mechanistic clues concerning the details of the amplification process in tumors. Viability was enhanced and reached 158% on 50 nm nanodot arrays, but dropped to 77.8% at 100 nm, and to 50% for

Table 2 VD_{50}, AD_{50}, FD_{50}, and CD_{50} of cell lines employed in the current study

Cell line	VD_{50}[a]/nm	VD_{75}/nm	AD_{50}[b]/nm	FD_{50}[c]/nm	CD_{50}[d]/nm	CD_{75}/nm
HELA	112	35	85	51	94	45
C33A	>200	68	>200	>200	>200	>200
ES2	>200	167	198	>200	>200	167
PA-1	108	37	147	72	142	85
TOV-112D	198	110	127	>200	>200	>200
TOV-21G	>200	167	>200	68	>200	152
MG63	196	164	143	>200	>200	184
NIH-3T3	71	26	75	110	148	99

[a] VD_{50} is defined as the diameter of nanodots on which 50% of the cell population remains viable compared to cells seeded on a flat surface after 3 days of incubation. VD_{50} for each cell line was derived by counting the number of cells on the nanodot arrays, drawing the graph of cell number *versus* dot diameter, and calculating the dot diameter at which 50% viability was obtained (Fig. 5). [b] AD_{50} is defined as the diameter of nanodots on which 50% of the cell population appears to have apoptosis-like morphology after a 3 day incubation. AD_{50} was calculated by counting the percentage of apoptotic cells on the nanodots, drawing the graph of percent apoptotic cell *versus* dot diameter, and calculating the dot diameter that causes 50% apoptosis (Fig. 6). [c] FD_{50} is the diameter of nanodots that promotes the formation of 50% of the focal adhesions compared to cells grown on a flat surface. FD_{50} was calculated by counting the number of vinculin stained spots per cell, drawing the graph of percent focal adhesions *versus* dot diameter, and finding the diameter that promotes 50% of the focal adhesions compared to the number present in cells grown on a flat surface (Fig. 6). [d] CD_{50} is the diameter of nanodots on which cells exhibit half the amount of microfilament bundles compared to cells grown on a flat surface. CD_{50} was calculated by counting the number of microfilament bundles per cell, drawing the graph of microfilament bundles *versus* dot diameter, and obtaining the diameter that reduces by half the number of microfilament bundles compared to cells grown on a flat surface (Fig. 7).

the 200 nm nanodot array. The cell morphology became more flat and extended at 50 nm, but mounted and changed to an apoptotic shape on 100 nm and 200 nm dot array surfaces. Immunostaining showed enhanced staining of vinculin, which represents enhanced cell adhesion, for nanodot sizes under 50 nm. The cytoskeleton organization loses its order when the nanodot size is larger than 100 nm. VD_{50}, AD_{50}, FD_{50}, and CD_{50} for TOV-21G are 196, 143, >200, and >200 nm, respectively. In summary, MG63 cells grew well and reached a maximized condition at 50 nm, but dropped back to normal levels if the size was larger than 100 nm.

Discussion

A nanodevice was fabricated that is capable of distinguishing the ability of cells to grow on various nanostructures. To better characterize this ability, four indices are defined. They are VD_{50}, AD_{50}, FD_{50}, and CD_{50}, which are intended to represent proliferation, apoptosis, cell adhesion, and cytoskeletal organization, respectively.

Two cervical cancer cell lines were screened, HELA and C33A. C33A represents a late-stage and advanced cancer, while HELA cells are less malignant in clinical stages. $VD_{50}/AD_{50}/FD_{50}/CD_{50}$ for HELA and C33A are 112/85/51/94 and >200/>200/>200/>200, respectively. The indices were consistent with the clinical stage and also with the *in vivo* invasive ability of cancer cells. The proliferation of HELA cells dropped, cells appeared apoptotic, and there was a loss of cell adhesion if the nanodot sizes were larger than 100 nm. However, the nanodot arrays did not affect the growth of C33A cells. C33A cells exhibited higher resistance to the nanostructures than HELA cells. Therefore, the nanodevice is capable of distinguishing the clinical stage and invasive ability of cancer cells.

There were four ovarian cancer cell lines tested, including clear cell carcinoma (ES2, TOV-21G), teratocarcinoma (PA-1), and endometrioid carcinoma (TOV-112D) cell lines. Grade 3/stage III carcinomas (TOV-112D and TOV-21G) were also tested. $VD_{50}/AD_{50}/FD_{50}/CD_{50}$ for ES2, TOV-21G, PA-1, and TOV-112D are >200/198/>200/>200, >200/>200/68/>200, 108/147/72/142, and 198/127/>200/>200, respectively. The results showed that PA-1 cells grew poorly if the nanodot size was larger than 100 nm, but the nanostructure did not significantly influence the ES2, TOV-21G, or TOV-112D cells. For ovarian cancer, the indices were consistent with the stage index and with the *in vivo* invasive ability of cancer cells. Although TOV-21G and TOV-112D are of the same grade, TOV-112D has a stronger invasive ability than TOV-21G. The nanodevice is therefore capable of determining the stage and invasive ability of two cell lines.

Definition of the indices used in the current study all maintained the convention of 50%, such as 50% viability. However, because nanostructures may not be as toxic as most other medical drugs, the definition might be modified to better distinguish the growth ability between cell lines. For example, $VD_{50}/AD_{50}/FD_{50}/CD_{50}$ for C33A and ES2 are >200/>200/>200/>200 and >200/198/>200/>200, respectively. If VD_{50}/CD_{50} is switched to VD_{75}/CD_{75}, then $VD_{75}/AD_{50}/FD_{50}/CD_{75}$ for C33A and ES2 are 68/>200/>200/>200 and 167/>200/>200/167, respectively (Table 2). C33A cells are apparently more viable but have more difficulty in adapting to novel nanostructures.

Parameters that promote cell growth and apoptosis can be derived instantly from our nanodevice. For example, HELA cells grow at a maximum when the diameter of the nanodots approaches 50 nm, but start to die (apoptose) if the diameter is larger than 100 nm. In dental implants, the biocompatibility between the implant and the osteoblasts determines the success of the operation and long-term maintenance. The parameters derived from the current study can provide pivotal information in design and fabrication of dental implants. In other cases, implants such as cardiovascular stents also require accurate control of the growth of epithelial cells and smooth muscle cells. The surface in contact with these live tissues can be designed to match the expected performance of the stents.

Conclusion

We have established a platform that can be used to assess basic parameters for cell growth. The specific platform could be used to observe the proliferation, apoptosis, adhesion, and

cytoskeletal organization of cells. The simplified fabrication process allows for mass production and lower costs. According to our results, the device is capable of distinguishing between cancer cell lines of various stages and also provides basic design parameters for artificial implants. Our device will serve as a convenient and fast tool for tissue engineering and cancer treatment.

Acknowledgements

This study was supported in part by the National Science Council in Taiwan (grants NSC96-2320-B-009-001 and NSC 97-2320-B-009-002-MY3), the Bureau of Animal and Plant Health Inspection and Quarantine Council of Agriculture in Taiwan (grant 98AS-9.2.4-BQ-B1), and by China medical university hospital (DMR-93-52 and DMR-97-075).

References

1 M. Bacac and I. Stamenkovic, *Annu. Rev. Pathol.: Mech. Dis.*, 2008, **3**, 221–247.
2 P. Friedl and K. Wolf, *Nat. Rev. Cancer*, 2003, **3**, 362–374.
3 U. Reuning, V. Magdolen, O. Wilhelm, K. Fischer, V. Lutz, H. Graeff and M. Schmitt, *Int. J. Oncol.*, 1998, **13**, 893.
4 W. G. Stetler-Stevenson, S. Aznavoorian and L. A. Liotta, *Annu. Rev. Cell Biol.*, 1993, **9**, 541–573.
5 M. R. Shen, C. Y. Chou and J. C. Ellory, *Pflügers Arch. Eur. J. Physiol.*, 2000, **440**, 751–760.
6 M. R. Shen, C. Y. Chou, K. F. Hsu, Y. M. Hsu, W. T. Chiu, M. J. Tang, S. L. Alper and J. C. Ellory, *J. Biol. Chem.*, 2003, **278**, 39941–39950.
7 K. Honda, T. Yamada, R. Endo, Y. Ino, M. Gotoh, H. Tsuda, Y. Yamada, H. Chiba and S. Hirohashi, *J. Cell Biol.*, 1998, **140**, 1383.
8 K. Honda, T. Yamada, Y. Hayashida, M. Idogawa, S. Sato, F. Hasegawa, Y. Ino, M. Ono and S. Hirohashi, *Gastroenterology*, 2005, **128**, 51–62.
9 N. Yamagata, Y. Shyr, K. Yanagisawa, M. Edgerton, T. P. Dang, A. Gonzalez, S. Nadaf, P. Larsen, J. R. Roberts and J. C. Nesbitt, *Clin. Cancer Res.*, 2003, **9**, 4695.
10 S. Yamamoto, H. Tsuda, K. Honda, T. Kita, M. Takano, S. Tamai, J. Inazawa, T. Yamada and O. Matsubara, *Mod. Pathol.*, 2007, **20**, 1278–1285.
11 G. Avila, K. Misch, P. Galindo-Moreno and H. L. Wang, *Implant Dent.*, 2009, **18**, 17.
12 C. H. Choi, S. H. Hagvall, B. M. Wu, J. C. Y. Dunn, R. E. Beygui and C. J. "Cj" Kim, *Biomaterials*, 2007, **28**, 1672–1679.
13 M. J. Cooke, S. R. Phillips, D. S. H. Shah, D. Athey, J. H. Lakey and S. A. Przyborski, *Cytotechnology*, 2008, **56**, 71–79.
14 E. Cukierman, R. Pankov, D. R. Stevens and K. M. Yamada, *Science*, 2001, **294**, 1708.
15 E. Fine, L. Zhang, H. Fenniri and T. J. Webster, *Int. J. Nanomed.*, 2009, **4**, 91.
16 A. Goransson, A. Arvidsson, F. Currie, V. Franke-Stenport, P. Kjellin, K. Mustafa, Y. T. Sul and A. Wennerberg, *J. Biomed. Mater. Res., Part A*, 2009, **88**, 1037.
17 D. A. Harrington, E. Y. Cheng, M. O. Guler, L. K. Lee, J. L. Donovan, R. C. Claussen and S. I. Stupp, *J. Biomed. Mater. Res., Part A*, 2006, **78**, 157.
18 T. Y. Lim, C. K. Poh and W. Wang, *J. Mater. Sci.: Mater. Med.*, 2009, **20**, 1669–1675.
19 J. Park, S. Bauer, K. von der Mark and P. Schmuki, *Nano Lett.*, 2007, **7**, 1686–1691.
20 S. Patel, K. Kurpinski, R. Quigley, H. Gao, B. S. Hsiao, M. M. Poo and S. Li, *Nano Lett.*, 2007, **7**, 2122–2128.
21 E. Rebollar, I. Frischauf, M. Olbrich, T. Peterbauer, S. Hering, J. Preiner, P. Hinterdorfer, C. Romanin and J. Heitz, *Biomaterials*, 2008, **29**, 1796–1806.
22 S. Sharma, V. P. Soni and J. R. Bellare, *J. Mater. Sci.: Mater. Med.*, 2009, **20**, 1427–1436.
23 J. Tan and W. M. Saltzman, *Biomaterials*, 2004, **25**, 3593–3601.
24 M. A. Wood, *J. R. Soc., Interface*, 2007, **4**, 1.
25 O. Zinger, K. Anselme, A. Denzer, P. Habersetzer, M. Wieland, J. Jeanfils, P. Hardouin and D. Landolt, *Biomaterials*, 2004, **25**, 2695–2711.
26 C. T. Wu, F. H. Ko and H. Y. Hwang, *Microelectron. Eng.*, 2006, **83**, 1567–1570.
27 R. Zaouk, B. Y. Park and M. J. Madou, *Methods Mol. Biol. (Totowa, N. J.)*, 2006, **321**, 17.

